JGR Atmospheres

RESEARCH ARTICLE
10.1029/2021JD036291

Climatology and Seasonal Variations of Temperatures and Gravity Wave Activities in the Mesopause Region Above Ft. Collins, CO (40.6°N, 105.1°W)

Chiao-Yao She[1], Zhao-Ai Yan[2,3], Chester S. Gardner[4], David A. Krueger[1], and Xiong Hu[2]

[1]Department of Physics, Colorado State University, Ft. Collins, CO, USA, [2]National Space Science Center, Chinese Academy of Sciences, Beijing, China, [3]University of Chinese Academy of Sciences, Beijing, China, [4]Department of Electrical & Computer Engineering, University of Illinois, Urbana, IL, USA

This article is a companion to Gardner et al. (2022), https://doi.org/10.1029/2021JD036387.

Key Points:

- With 956 nights of observations, we revisit the climatology of the background temperature and study seasonal gravity wave (GW) activities
- Sharp transitions are found at Days 121 and 222 between the higher radiation-driven and the lower dynamic-driven mesopauses at 40.6°N
- The winter GW potential energy is ~40% higher than other seasons. Climatologically, their profiles suggest wave breaking below 85 km

Correspondence to:
C.-Y. She,
joeshe@colostate.edu

Citation:
She, C.-Y., Yan, Z.-A., Gardner, C. S., Krueger, D. A., & Hu, X. (2022). Climatology and seasonal variations of temperatures and gravity wave activities in the mesopause region above Ft. Collins, CO (40.6°N, 105.1°W). *Journal of Geophysical Research: Atmospheres*, *127*, e2021JD036291. https://doi.org/10.1029/2021JD036291

Received 20 DEC 2021
Accepted 2 MAY 2022

Author Contributions:
Conceptualization: Chiao-Yao She, Chester S. Gardner
Formal analysis: Zhao-Ai Yan, David A. Krueger
Funding acquisition: Zhao-Ai Yan, Chester S. Gardner, Xiong Hu
Methodology: Chiao-Yao She, David A. Krueger
Project Administration: Chiao-Yao She
Resources: Xiong Hu
Software: Zhao-Ai Yan, David A. Krueger
Validation: Chiao-Yao She, Zhao-Ai Yan
Writing – original draft: Chiao-Yao She

Abstract Utilizing 956 nights of Na lidar nocturnal mesopause region temperature profiles acquired at Fort Collins, CO (40.6°N, 105.1°W) over a 20-year period (March 1990–2010), we deduce background nightly mean temperature $\overline{T}(z)$ and the square of the buoyancy frequency $N^2(z)$ at 2-km resolution between 83 and 105 km. The temperature climatology reveals the two-level mesopause structure with clarity and sharp mesopause transitions, resulting in 102 days of summer from Days 121 to 222 of the year. The same data set analyzed at 10-min and 1-km resolution gives the gravity wave (GW) temperature perturbations $T_i'(z)$ and the wave variance $Var(T'(z))$ and GW potential energy $E_{pm}(z)$ between 85 and 100 km. Seasonal averages of GW $Var(T'(z))$ and $E_{pm}(z)$ between 90 and 100 km, show that $Var(T')$ for spring and autumn are comparable and lower than for summer and winter. Due mainly to the higher background stability, or larger $N^2(z)$ in summer, $E_{pm}(z)$ between 85 and 100 km is comparable in spring, summer, and autumn seasons, but ~30%–45% smaller than the winter values at the same altitude. The uncertainties are about 4% for winter and about 5% for the other three seasons. The values for E_{pm} are (156.0, 176.2, 145.6, and 186.2 J/kg) at 85 km for (spring, summer, autumn, and winter) respectively, (125.4, 120.2, 115.2, and 168.7 J/kg) at 93 km, and (207.5, 180.5, 213.1, and 278.6 J/kg) at 100 km. Going up in altitude, all profiles first decrease and then increase, suggesting that climatologically, GWs break below 85 km.

1. Introduction

Based on observations at a polar site (69°N), Lübken and von Zahn (1991) reported a counter-intuitive bistable pattern of mesopause, high in winter (192K at 98 km) and low in summer (129K at 88 km). Though unexpected, Na lidar observations showed that the bistable pattern also exists in a midlatitude station (40.6°N) with winter mesopause at 101 km and summer mesopause at 86 km (She et al., 1993; Yu & She, 1995). The two-level mesopause was further confirmed by shipborne K lidar observations (von Zahn & Höffner, 1996), which enabled observations between 71°S and 54°N from late April to early July 1996. This set of measurements which included southern and northern equatorial regions showed that the summer state does not exist in the equatorial region. Using 2 years of data (1996–1997) from Fort Collins (40.6°N, 105°W) and Kühlungsborn, Germany (54°N, 12°E), along with older monthly mean data from ALOMAR, Norway (69°N, 16°E), the concept of the two-level mesopause was further elucidated (She & von Zahn, 1998) and idealized in Figure 1 of their paper. They asserted the two-level mesopause structure exists globally in midlatitude and polar regions but not in equatorial regions. In the two-level structure, there exists an altitude of minimum annual variation in temperature near 98 km and an altitude of maximum annual variation in temperature near 86 km. There also exists a high-altitude winter mesopause near 100 km and a low-altitude summer mesopause near 88 ± 3 km with a clear and abrupt jump between them, despite of the fact that unlike at 69°N and 54°N, the sharp summer/winter transitions were not observed at 40.6°N. The less clear summer/winter mesopause transition at 40.6°N is due to the relatively smaller difference between summer and winter mesopause temperatures at a lower-latitude station, which may be over-powered by superimposed day-to-day wave perturbations in a 2-year data set. However, when the true climatology of the temperature structure is revealed, the proposed two-level mesopause structure with sharp winter/summer transitions can be ascertained. One objective of this paper is to use the 20 years (956 nights) of nocturnal temperature observations to investigate the climatology of the two-level mesopause and to reveal the sharp mesopause transitions at midlatitude.

Writing – review & editing: Chester S. Gardner, David A. Krueger

The important roles that atmospheric gravity waves (GWs, which include solar tides) play in mesosphere and lower thermosphere (MLT) is well known and articulated in the literature (e.g., Fritts & Alexander, 2003). Notably, they lead to cold summer mesopause and residual circulation from the summer pole to the winter pole (Hitchman et al., 1989; Lindzen, 1981; Yuan et al., 2008). Lidars have become an instrument of choice for GW studies; their dynamics, fluxes, and effects on atmospheric stability have recently been reviewed by Alan Liu in a book chapter, entitled "MLT Science Enabled by Atmospheric Lidars" (She et al., 2021). Their statistical characterization to better quantify the climatology, heat, and momentum fluxes, as well as possible long-term trends however requires ample high-resolution observational data, which is more difficult to achieve. Rayleigh lidar has been used by Wilson et al. (1991) to track the climatological activities of GWs between 30 and 75 km with 100 nights of observation (3 or 4 hr a night) in 4 years (1986–1989) at Haute-Provence Observatory (OHP; 43.93°N, 5.71°E). They found annual oscillation (AO) dominance with maximum GW potential energy (per unit mass) E_{pm} in winter and minimum in summer in upper stratosphere and lower mesosphere (30–60 km) where signal-to-noise is good. In the middle mesosphere (60–75 km), they found semiannual oscillations (SAOs) again with max in winter along with summer value higher than spring and autumn amid large scatters in data. Using more data between 1996 and 2012 with temporal resolution of 26 min and vertical resolution of 1.5 km (30–50 km) or 3 km (50–85 km), Mze et al. (2014) reached the same conclusion on the midlatitude seasonal distribution of GW activities. GW activities over Toronto (44°N, 80°W) were reported by Whiteway and Carswell (1995) with 1 year of 130 nights of observation between 35 and 50 km with temporal resolution of 30 min; they also reported a seasonal variation with a winter maximum and summer minimum for GW potential energy, a result consistent with the OHP observations. In the polar region, a comprehensive study of stratospheric GWs (30–50 km) at McMurdo (77.8°S, 166.7°E) from 5 years (2011–2015) of lidar observation with 354 data segments, each between 6 and 12 hr observation has appeared recently (Chu et al., 2018). They also reported annual variation with summer minimum and winter maximum. Investigating GWs with periods between 10 min and 8 hr in the mesosphere (67–80 km) with Adelaide MF radar (35°S), Saskatoon MF radar (52°N) and the MU radar at Shigaraki (35°N), Nakamura et al. (1996) reported SAO in wind velocity variance with maxima in solstices and minima in equinoxes. Rauthe et al. (2008) used combined Rayleigh-Mie-Raman lidar and potassium lidar to cover an extensive altitude range between 1 and 105 km at Külungsborn (54°N) and reported GW potential energy E_{pv} (per volume) between 20 and 100 km with 15 min and 1 km resolution in 236 nights (with a minimum duration of 3 hr per night) between June 2002 and October 2006. They showed AO in potential energy with winter maximum and summer minimum for all altitudes. The winter-summer difference in GW potential energy is believed to be the result of critical-level filtering of GWs by the prevailing winds (Chu et al., 2018; Lindzen, 1981; Whiteway & Carswell, 1995; Wilson et al., 1991) that blocks much of the westward and stationary GWs from entering (with only high speed eastward waves transmitting into) stratosphere and lower mesosphere in summer, while only eastward GWs are blocked with stationary and westward wave transmission in winter. The situation is apparently different in the tropics. Li et al. (2010) analyzed 10.5 years temperature data from MLO Rayleigh lidar in Hawaii (19.5°N, 155.6°W) with 30 min and 0.3 km resolution and reported AO dominance in total GW variance in the upper stratosphere (35–50 km) resulting from filtering by the wind in the troposphere and lower stratosphere. However, in the lower mesosphere (48–63 km), the GW variance was dominated by SAO, likely due to the selective filtering of GWs by the tropical upper stratospheric SAO wind. Very recently, Strelnikova et al. (2021) compared GW potential energies from Kühlungsborn (54°N, 12°E) and ALOMAR, Norway (69°N, 16°E) based on 7 years of lidar data with 1 hr resolution and filtered to vertical wavelength ($\lambda z < 15$ km) and period ($\tau < 8$ hr). They reported annual cycle with winter maximum in both stations and showed potential energy density (per volume) Epv at Kühlungsborn about a factor of 2 higher than at ALOMAR.

Most of these works ascertain the presence of semiannual variation by utilizing a scatter plot of annual distribution of GW activity to visually determine whether summer activity is stronger than that of spring and autumn. Since both annual and semiannual variations exist in GW activities, with sufficient data, a better alternative is to decompose the wave perturbation profiles throughout the year into annual mean, annual and semiannual variations and then compare their amplitudes. This is the approach used by Gardner and Liu (2007) for their mesopause region GW study. With 956 nights of temperature observations, we will investigate GWs activities in terms of annual mean and harmonic components with 12-month, 6-month, 4-month, and 3-month periods in this paper.

Lidar study of GW activities in the mesopause region (80–110 km) is rare in part because of the need to use the more challenging narrowband metal resonance lidars, Na lidar (Fricke & von Zahn, 1985; She et al., 1990), K lidar (von Zahn & Höffner, 1996), or Fe lidar (Lautenbach & Höffner, 2004). Other than the observation by the

potassium lidar mentioned above (Rauthe et al., 2008), the study of seasonal variations in GWs by Gardner and Liu (2007) is the most comprehensive. They reported temperature and wind profiles as well as the associated wave perturbation variances and covariances to characterize the climatology as well as the vertical fluxes of heat and horizontal momentum. The unique 3.5 m telescope at the Airforce's Starfire Optical Range (SOR), NM (35.0°N, 106.5°W) that this lidar utilized made it possible to measure temperature and wind profiles in five Cardinal directions with 0.5 km and 90-s resolution. Although they only have 49 nights of data, they are well distributed seasonally to facilitate good seasonal variation studies of the quantities associated with the GW activity. They analyzed the wave activities in terms of annual mean, 12-month and 6-month variations, and found that the wind and temperature variances between 85 and 100 km exhibit strong 6-month oscillations with maximum downward fluxes during summer and winter. Another GW climatology in the literature is the paper by Yue et al. (2018), reporting the seasonal variation of GW potential energy E_{pm} (per unit mass) over the Arecibo Observatory in tropical Puerto Rico (18.4°N, 66.8°W) with 198 nights of potassium lidar observation with 0.9 km and 30 min resolution. They reported comparable annual and semiannual variation amplitudes in GW potential energy. Very recently, Guo and Liu (2021), based on 118 nights of Na lidar observation over 4+ years at Cerro Pachon (30.3°S, 70.7°W), have reported seasonal variation of $Var(T')$, vertical heat, and energy fluxes. In Figure 2a, they reported values for $Var(T')$ ranges from ~40 K^2–~90 K^2.

There are 20 years of temperature data collected from the Na lidar deployed at the Foot Hill campus of Colorado State University (CSU) in Fort Collins, CO (40.6°N, 105.1°W). A total of 956 nights of data, 4–14 hr observation per night, were collected and are evenly distributed in spring, summer, autumn, and winter with 236, 229, 274, and 217 nights of observation, respectively. Though the power-aperture product of this lidar is smaller than the lidar at SOR, thus requiring 10-min integration for good temperature measurements with vertical resolution of 1 km, the abundant observations make it attractive for the study of climatology and seasonal variations of background temperature and GW activities. Thus, after a brief discussion of the climatology of nocturnal temperature, the main purpose of this paper is to investigate the climatology of midlatitude MLT GW activities from this 20-year-long data set. This paper describes the data set and atmospheric parameter of interest, associated with background temperatures and GW perturbations in Section 2, shows the resulting climatology of background temperature in Section 3 and the seasonal variations of GW perturbations and potential energy in Section 4. This is followed by a discussion in Section 5 and conclusion in Section 6. The data processing technique is described in Appendix A and examination on the goodness of climatological fits in Appendix B.

2. The Data Set and Atmospheric Parameters of Interest

The CSU Na lidar performed mesopause region observations between March 1990 and 2010 at Fort Collins, CO (40.6°N, 105.1°W). A vertical beam between 1990 and 2001 measured mesopause region Na density and temperature using the two-frequency technique (She et al., 1990). In 2002, the lidar was upgraded to two-beam or three-beam geometry, pointing 20° or 30° off zenith, for simultaneous Na density, temperature, and horizontal wind measurements (both day and night weather permitting) using the three-frequency technique (She & Krueger, 2007; She & Yu, 1994). The raw photon files are collected at slant length resolution of 150 m, either two photon files (for two-frequency measurements) or three photon files (for three-frequency measurements) in 1-min or 2-min' time. Only nocturnal observations are used for this study.

The raw photon files are then processed to yield observed temperatures (Krueger et al., 2015) or temperature perturbations with either nightly or 10-min integration and vertically smoothed by a running Hanning window with FWHM width of 2 or 1 km, respectively. The nightly mean temperatures observed from each beam are available from (Madrigal Database at Millstone Hill) and the high resolution (10 min mean) temperatures of each available beam were accessed from (Digitalcommons of Utah State University). For the nights with two-beam or three-beam operation, the temperatures (and associated uncertainties) at a given altitude are averaged by inverse-error-square weighting to make the measurement with smaller uncertainty more dominant. For simplicity and consistency, we simply use the first portion (956 nights of observation acquired from the CSU site between March 1990 and 2010) of the Pinatubo effect removed nightly mean temperature profiles used in the recent long-term temperature trend studies (She et al., 2019) as the background temperatures $\overline{T}(z)$ and associated uncertainty $\Delta\overline{T}(z)$ for this study. Briefly, the removed Pinatubo warming episode began immediately after the volcanic eruption in June 1991. It reaches a peak in the beginning of 1993, lingering about 7 years before it decays away. The peak warming increases as altitude increases from ~8K at 88 km to ~19K at 103 km as shown clearly in Figure 3a

of She et al. (2015). The temperature data used in this work has not been detrended for the long-term temperature trends. Using these temperatures, we calculate the nightly mean lapse rate $-d\overline{T}(z)/dz$ and uncertainty $\Delta[-d\overline{T}(z)/dz]$, from which the buoyancy frequency square $N^2(z) = g(d\overline{T}/dz + \Gamma_d)/\overline{T}$ and gamma square $\Gamma^2(z)=(d\overline{T}/dz + \Gamma_d)^2$ may be derived along with their respective uncertainties $\Delta[N^2(z)]$ and $\Delta[\Gamma^2(z)]$. Here $g = 9.5 \times 10^{-3}$km/s^2 and $\Gamma_d = 9.5$K/km are gravitational acceleration and adiabatic lapse rate at MLT, respectively.

The high-resolution temperature profiles $T(z,t_i) \equiv T_i(z)$ at a time interval i, on the other hand are data with 10-min integration and vertically smoothed to 1 km resolution (sampled at 0.5 km interval); these are used to deduce wave perturbations $T'(z,t_i) = T'_i(z)$ by the method described in Appendix A. Using these deduced wave perturbations $T'_i(z)$, we can calculate the nightly mean variance of wave perturbations $Var(T'(z)) = <(T'(z))^2>$ and associated photon noise uncertainty $<(\delta T(z))^2>$, as well as the nightly mean variances of the gradient perturbations, $Var(dT'(z)/dz) = <(dT'(z)/dz)^2>$and associated uncertainties, to be used in the companion paper (Gardner et al., 2022).

In this study, we are also interested in the potential energy of wave perturbations. The potential energy of a unit mass harmonic oscillator is $E_{pm} = 0.5\omega 2\overline{\varsigma^2}$, where $\overline{\varsigma^2}$ is the mean square rms (or variance of) displacement, and ω is the angular frequency. In the context of atmospheric waves, we consider an air parcel of unit mass in hydrostatic equilibrium, oscillating with vertical displacement ς relative to an equilibrium position. The relevant angular frequency denoted as N, is the buoyancy frequency of parcel's vertical movement. Since the fractional temperature perturbations $\langle(T'/\overline{T})^2\rangle$is related to the rms vertical displacement square $\overline{\varsigma^2}$, the potential energy (per unit mass) of the wave oscillation E_{pm}, following Wilson et al. (1991), may also be expressed in terms of gravity acceleration g, (angular) buoyancy frequency square $N^2$and $\langle(T'/\overline{T})^2\rangle$as in Equation 1a below; its associated percentage uncertainty $\Delta(E_{pm})$ as Equation 1b below:

$$E_{pm} = \frac{1}{2}N^2\overline{\varsigma^2} = \frac{1}{2}\left(\frac{g}{N}\right)^2 < \left(\frac{T'(z)}{\overline{T}(z)}\right)^2 > \text{with } N^2 = \frac{g}{\overline{T}}\left(\frac{d\overline{T}}{dz} + \frac{g}{c_p}\right) = \frac{9.5 * 10^{-3}}{\overline{T}}\left(\frac{d\overline{T}}{dz} + 9.5\right) \quad (1a)$$

$$\frac{\Delta(E_{pm})}{E_{pm}} = 100 * \sqrt{\left(\frac{\Delta Var(T')}{Var(T')}\right)^2 + \left(\frac{\Delta(N^2)}{N^2}\right)^2 + \left(\frac{\Delta(\overline{T})}{\overline{T}}\right)^2} \; in\ \%;\ \frac{\Delta\left(N^2\right)}{N^2}$$
$$= \sqrt{\left(\frac{\Delta\overline{T}}{\overline{T}}\right)^2 + \frac{\left(\Delta\left[\frac{\partial\overline{T}(z)}{\partial z}\right]\right)^2}{\left(\frac{d\overline{T}}{dz} + 9.5\right)^2}} \quad (1b)$$

where $g = 9.5$ ms^{-2}, $c_p = 1005$ JK^{-1} kg^{-1} are respectively earth gravitational acceleration and unit mass heat capacity in the mesopause region and $d\overline{T}/dz$, vertical temperature gradient in units of K/km.

3. Climatology of Background Temperature and Buoyancy Frequency Square

As mentioned earlier, the nightly mean (background) temperature profiles $\overline{T}(z)$ (sampled at 0.5 km interval in 2 km resolution) between March 1990 and March 2010 is taken from the data set used in the recent long-term temperature trend studies (She et al., 2019), from which we calculate the nightly mean profiles of buoyancy frequency square $N^2(z)$. To investigate the seasonal variations (climatology) of $\overline{T}(z)$ and $N^2(z)$, we perform regression analysis of the data time series in question to a fit function $F(t)$ of linear superposition of a constant and sinusoidal variations with periods of 12-month, 6-month, 4-month, and 3-month at each altitude as:

$$F(t) = A + \sum_{i=12,6,4,3} C_i \cos(2\pi t/\tau_i) + S_i \sin(2\pi t/\tau_i) :\ \tau_{12} = 1.0;\ \tau_6 = 0.5;\ \tau_4 = 1/3;\ \tau_3 = 0.25 \quad (2)$$

Once the fit parameters A, C_i, and S_i, and associated uncertainties are determined from the above linear regression fit, we can deduce the amplitude and phase (maximum) profiles as well as the best-fit nightly mean profiles in question. Using these results, we can display the month-altitude contours and profiles of annual mean along with harmonic amplitudes with periods of 12-month, 6-month, 4-month, and 3-month of background temperature $\overline{T}$ and buoyancy frequency square N^2 as well as the derived quantities. As in She et al. (2000), we display analysis

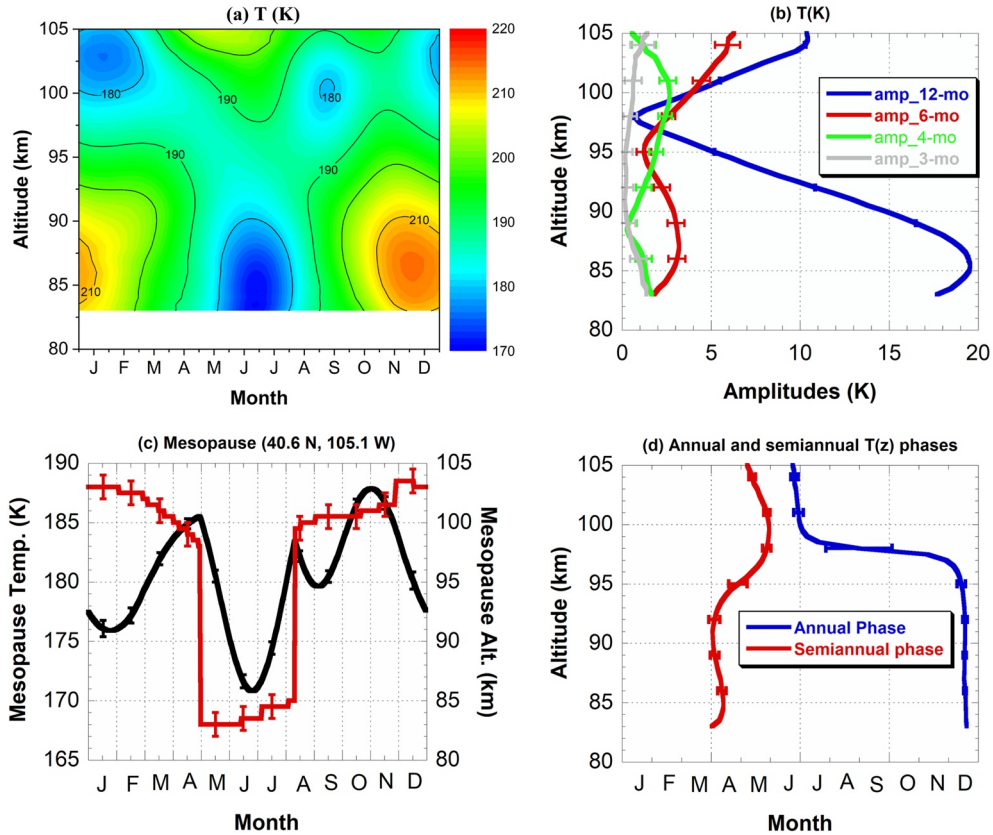

Figure 1. (a). Month-altitude contours derived from the annual mean, 12-month, 6-month, 4-month, and 3-month harmonic fit to lidar temperature observations made from March 1990 to 2010 at Ft. Collins, CO. (b). Seasonal harmonic amplitude profiles with the period of 12 (blue), 6 (red), 4 (green), and 3 (gray) months. (c). Annual time series of mesopause altitudes (red) and mesopause temperatures (black), and (d). Annual (blue) and semiannual (red) phase, derived from the data plotted in (a).

results for $\overline{T}(z)$ and $N^2(z)$ between 83 and 105 km due to photon noise considerations. An example on the fitting variability is shown in Figure A3a, Appendix B.

3.1. Month-Altitude Contours and Amplitudes of Seasonal Harmonics of Background Temperatures

The month-altitude contour plot and profiles of harmonic amplitudes with periods of 12-month, 6-month, 4-month, and 3-month of the background temperature $\overline{T}$ are shown respectively in Figures 1a and 1b. This harmonic analysis with 20 years of data smooth out all other transient perturbations but the annual means and perturbations with the period of 12-month, 6-month, 4-month, and 3-month. The background temperature contour, Figure 1a may be compared to Figure 3a of She et al. (2000) based on 8 years of data between 1990 and 1999. The general features of the two contours are the same. The expected two-level mesopause is clearly seen in both. The annual mean temperature profile shown in red in Figure 3a, also compares favorably to the top panel of Figure 3a of She and von Zahn (1998) based on 1996/1997 data, while the annual mean temperature in She et al. (1995) based on early 3 years (1991–1993) data appears to be higher by ~5K due to Mt. Pinatubo warming (She et al., 1998). The profiles of annual and semiannual amplitudes remain nearly the same between current work and earlier publications.

Unlike at a higher-latitude site, Kühlungsborn (54°N, 69°N), the transition between winter and summer mesopause altitudes over Fort Collins (40.6°N) based on 2 years of data, are not clear (She and von Zahn, 1998). These transitions became clear and sharp when the annual temperature variations were displayed in a contour based on 8 years of observation (She et al., 2000). The two-level mesopause structure at this midlatitude station based on the best harmonic fit to 20 years data shown in Figures 1a and 1c is now very clear. Analysis of the contour plot time series at 0.5 km altitudes indeed showed that the altitude with maximum temperature variation occurs at 85.5 km

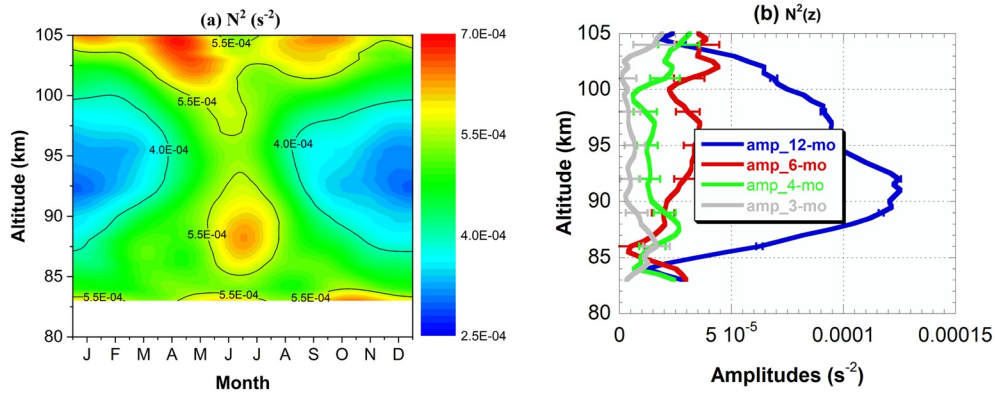

Figure 2. (a) and (b). Same as Figures 1a and 1b, respectively, except for buoyancy frequency square, $N^2(z)$.

with temperature variation from 171.0 to 213.9K ($\Delta T = 42.9$ K) and that the altitude with minimum temperature variation occurs at 98 km with temperatures variation from 181.7 to 191.2K ($\Delta T = 9.5$ K). The associated extrema in annual amplitudes shown in blue in Figure 1b are 19.5 ± 0.5K at 85.5 km and 0.7 ± 0.4K at 98 km. This may be compared to extrema in annual amplitudes in higher-latitude site, Kühlungsborn (54°N), based on 5 years of data (Gerding et al., 2008), with maximum of 27.5K at 85 km and minimum of 3K at 102 km. To discern mesopause temperatures and mesopause altitudes better, we use the data of the contour plot, Figure 1a, in daily time series at 0.5 km interval, to determine mesopause altitudes and mesopause temperatures; they are shown respectively in red and black in Figure 1c. The most striking feature in this figure is the sharp mesopause altitude transitions leading to a 102-day summer season at 40.6°N between Days 121 (May 1) and 222 (August 10) of the year. The summer mesopause altitude is nearly a constant, statistically at 83.7 ± 0.7 km with 0.7 km being its standard deviation. Since the vertical resolution of our background temperature is 2 km, the summer mesopause is then at 84 ± 1 km. The winter mesopause altitude, unlike the idealized prediction given in Figure 1 of She and von Zahn, (1998), varies between 98 and 103.5 km; statistically, it is at 101.4 ± 1.4 km. For a higher-latitude site at 54°N, the sharp transitions are clear even in scatter plot with 2 years of data with summer lasting for almost 4 months, see Figure 4b of She and von Zahn, (1998). More recent data (see the upper-right panel of Figure 8 in Gerding et al., 2008) show clear bi-stable state with the mesopause in the lower level (at ~86 km) for about 120 days between May and August and in the high level (at ~102 km) for the rest of the year. The annual variation in mesopause temperatures appears to have similar shape with relative maxima and minima occurring at nearby days between the two sites at different latitudes, see the lower-right panel of Figure 8 in Gerding et al. (2008) and Figure 1c here, although the minimum of the mesopause temperature, both occurring in June, it is 171K at 40.6°N and 142K at 54°N. It is also interesting to compare these nocturnal observations to the mesopause based on full-diurnal-cycle (24 hr

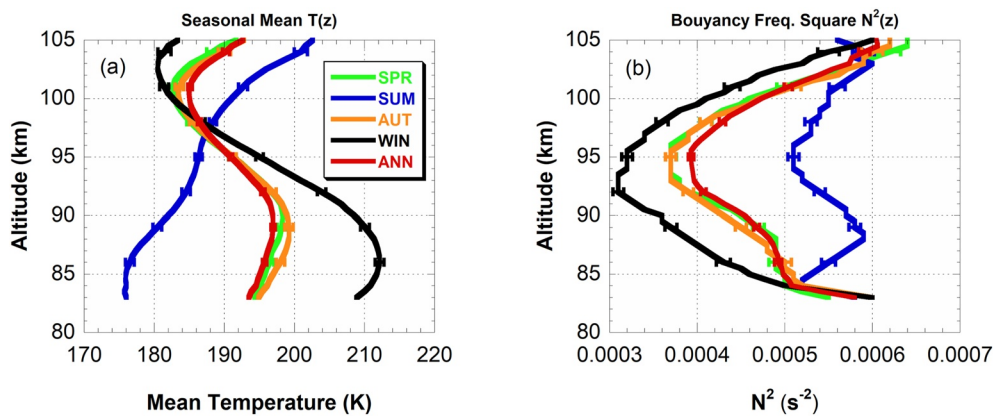

Figure 3. (a). Annual and seasonal mean profiles of background temperatures $T(z)$, Annual (red), Spring (green), Summer (blue), Autumn (brown), and Winter (black). (b). Same as (a), except for buoyancy frequency square, $N^2(z)$.

continuous) observations. Examining the monthly mean temperature as a function of altitude as shown in Table 1a of Yuan et al. (2008), the bistable state of mesopause altitudes is clear with ~3 months in the lower/summer state. The maximum upper mesopause temperature also occurs in the months of October (179K) and November (184K). The high mesopause temperature variation at another lower-latitude site, Starfire Optical Range (SOR), N.M. (35°N), see Figure 12 of Chu et al. (2005), is like that of Fort Collins (40.6°N), except without the Oct/Nov increase. The prominent minimum in lower mesopause temperature in Jun/Jul, resulting from the upwelling of the residual circulation, exists in all three sites. The temperature variation in winter mesopause is more complicated. We believe the seasonal variation of mesopause temperature is the result of the interplay between adiabatic heating/cooling associated with the residual circulation system and the variation of insolation throughout the year. Invoking on the observed climatology of meridional wind over Fort Collins, shown in Figure 3h of Yuan et al. (2008), we may explain the seasonal variation of mesopause temperature over Fort Collins qualitatively. In summer the upwelling (with the peak southward meridional wind of about 16 m/s at ~85 km in May/June) overwhelms the effect of insolation and cools the mesopause, leading to the prominent mesopause temperature minimum in June/July. As we move into fall, this cooling weakens, and the adiabatic heating begins as the winter downwelling begins gradually to the peak northward meridional wind of about 5 m/s at ~95 km in November/December. This gradual warming along with the reduction of insolation as we move toward winter solstice leads to a maximum mesopause temperature in October/November, after this point toward winter solstice, insolation is reduced faster than the gradual increase of downwelling heating. The April/May (August/September) mesopause temperature maxima result from the combined effects of the reduction (gradual increase) in adiabatic heating and increasing (decreasing) insolation in the spring (fall). Interestingly, the observed meridional wind switching direction for about a month in January at 95 km could account for the second mesopause temperature minimum in January, as shown in Figure 1c. All these characteristics of the midlatitude mesopause are consistent with the idealized prediction depicted in Figure 1 of She and von Zahn (1998), that is, the climatology of mesopause in MLT background temperatures has two seasons, winter, and summer with sharp transitions. Though the observed mesopause altitude in summer is a constant within experimental error, consistent with the prediction in their Figure 1b, the winter mesopause temperatures at 40.6°N varies between 176 and 188K, far from being an idealized constant (~210 K) as depicted in their Figure 1a. Another unique feature of the mesopause region temperature is now well-known, counter-intuitive with summer colder than winter. This counter-intuitive temperature structure shown in Figure 1a, as well as in the annual temperature phase plot in Figure 1d, reveal an out of phase annual temperature maxima in December below 98 km with an abrupt switching at about 98 km in June–July to be in-phase with solar heating. The annual and semiannual temperature phases shown in Figure 1d are consistent with that in the top panel of Figure 3c in She and von Zahn (1998), except with much smaller uncertainties. Using combined data from Na and Rayleigh lidars, the height range of the counter-intuitive thermal structure at midlatitudes appears to be between 65 and 98 km, see Figure 4b of She et al. (1995). This is consistent with the altitude range of the annual phase reversal between 65 and 101 km at 54°N, see Figure 8 in Gerding et al. (2008).

3.2. Month-Altitude Contours and Amplitudes of Seasonal Harmonics of N^2

The potential energy of atmospheric wave oscillation of a unit mass air parcel, according to Equation 1a is proportional to the square of rms vertical displacement $\overline{\varsigma^2}$, that is, $E_{pm} = 0.5\mathrm{N}^2\overline{\varsigma^2}$. E_{pm} is also proportional to the variance of fractional temperature perturbations, $\langle(\mathrm{T}'/\overline{T})^2\rangle$, that is, $E_{pm} = 0.5(\mathrm{g/N})^2\langle(T'/\overline{T})2\rangle$, leading to $\overline{\varsigma^2} = (\mathrm{g/N}^2)^2\langle(T'/\overline{T})^2\rangle$, also termed normalized $Var(T')$ as shown in Equation A3. For a given energy E_{pm}, the rms displacement would be smaller and fractional temperature perturbations larger in a more stable atmosphere, that is, larger $N^2(z)$. As a parcel moves adiabatically (constant E_{pm}) in a more stable background, it experiences a larger restoring force (buoyancy), corresponding to a larger difference between air parcel and its environment, that is, larger $\langle(T'/\overline{T})^2\rangle$. The wave perturbations diminish as atmosphere becomes convectively unstable. From the month-altitude contours and seasonal mean of amplitude profiles of $N^2(z)$, shown respectively in Figures 2a and 2b, it is clear that the values of $N^2(z)$ are larger in summer than in winter, especially so between 85 and 100 km. A consequence of high atmospheric stability in summer is relatively lower the GW's E_{pm} and $\overline{\varsigma^2}$ in summer. Indeed, we note at a given altitude, SUM >> WIN in $N^2(z)$ in Figure 3b corresponds to SUM << WIN in E_{pm} and $\overline{\varsigma^2}$, as shown, respectively in Figure 5b below and in Figure 3b of the companion paper (Gardner et al., 2022), while SUM ~ WIN in $Var(T')$ in Figure 5a, between 90 and 100 km below.

3.3. Seasonal Mean Profiles of $\overline{T}(z)$ and $N^2(z)$, and Associated Uncertainties

From the fit functions of $\overline{T}(z)$ and $N^2(z)$ and associated uncertainties, we compute the four seasonal (each centered at the respective equinox or solstice) mean profiles of background temperature and buoyancy frequency square. The measured seasonal mean temperatures are quite accurate; as shown in Figure 3a, with measurement uncertainty varying between 0.3% and 0.7%. The temperature structure is counter-intuitive, as summer is colder than winter between 83 and ∼98 km. The spring, autumn, and winter showed high mesopause, near 100–103 km in winter, while in summer it shows low mesopause at ∼84 km, consistent with the idealized two-level mesopause, see She and von Zahn (1998), along with maximum temperature variation at 86 km and with minimum annual temperature variation at ∼98 km. The atmosphere is more stable in summer and less stable in winter while spring and autumn are in between as shown by $N^2(z)$ between 84 and 102 km in Figure 3b with the fitting uncertainties between 1% and 2%. The climatological seasonal averages of $\overline{T}(z)$ and $N^2(z)$ are tabulated at 1-km intervals in Table 1.

4. Climatology and Seasonal Means of Gravity Wave Perturbations and Potential Energy

We now turn to the variance of temperature GW perturbations $Var(T')$ and the associated potential energy per unit mass E_{pm}. As in Section 3, we first perform the regression fits to the 20-year data time series of $Var(T')$ and E_{pm}. An example of the fitting variability, is shown in Figure A3b, along with discussion in Appendix B. With the respective climatological best fits, we present their contour plots and the associated seasonal harmonic amplitudes. To better reveal their seasonal differences, we then present the seasonal average profiles from the respective fit functions $F(t)$, both between 85 and 100 km due to signal-to-noise considerations.

4.1. Month-Altitude Contours and Seasonal Harmonic Amplitudes of $Var(T')$ and E_{pm}

The contour plot of wave perturbation variance $Var(T')$, shown in Figure 4a, clearly reveals semiannual variation with solstice maxima and equinox minima. The semiannual amplitude between 91 and 98 km, shown as red in Figure 4b is more than a factor of 2 larger than the annual amplitude (in blue), consistent with data at Starfire Optical Range (SOR), N.M. (35°N, 106.5°W) in Figure 5b of Gardner and Liu (2007), but both the SOR 12-month and 6-month amplitudes are more than twice larger. Unlike the wavier SOR annual mean, the $Var(T')$ annual mean over Fort Collins, CO (40.6°N, 105.1°W) shows a clear decreasing/increasing trend, from ∼68 K^2 at 85 km decreasing to ∼41 K^2 at ∼93 km and then increasing to ∼70 K^2 at 100 km, as shown in red in Figure 5a.

The month-altitude contour of waves' potential energy E_{pm} as shown in Figure 4c has similar appearance as that of Var (T′), except a noticeable qualitative difference of an additional minimum occurring in the months of June and July due to the highly stable background atmosphere (or large N^2) above the low summer mesopause as shown in Figure 2a, resulting in annual amplitude comparable and slightly larger than semiannual amplitude between 87 and 95 km, as shown in Figure 4d. Contrary to $Var(T')$, the annual amplitudes of E_{pm} between 95 and 100 km are larger than the semiannual amplitudes by ∼40%. The potential energy annual mean, shown in red in Figure 5b, decreased from ∼166 J/kg at 85 km to a minimum of about 127 J/kg at ∼90 km, implicating wave breaking below 85 km with annual mean damped against a background of decreasing air density that adiabatically amplifies wave amplitudes. The two effects reach a balance at ∼90 km and the annual mean increases again at higher altitudes to ∼220 J/kg at 100 km. Comparing the annual means (red curves) in Figures 5a and 5b between 100 and 85 km, we note the former is larger than the latter by ∼3% for $Var(T')$ and by ∼30% for E_{pm}.

4.2. Seasonal Mean Profiles of $Var(T')$ and E_{pm}, and Associated Uncertainties

The seasonal difference in $Var(T')$ and E_{pm} can better be seen in the respective seasonal average of the respective fit functions $F(t)$ at each altitude. For this purpose, we divide a year of individual fit function into four seasons, each centered at the respective equinoxes or solstices. The seasonal averaged profiles and the associated uncertainties are then calculated and displayed in Figure 5a for $Var(T')$ and in Figure 5b for E_{pm}. The profile of spring (SPR) and autumn (AUT) seasons are roughly the same for E_{pm} and for $Var(T')$ only between 90 and 100 km with

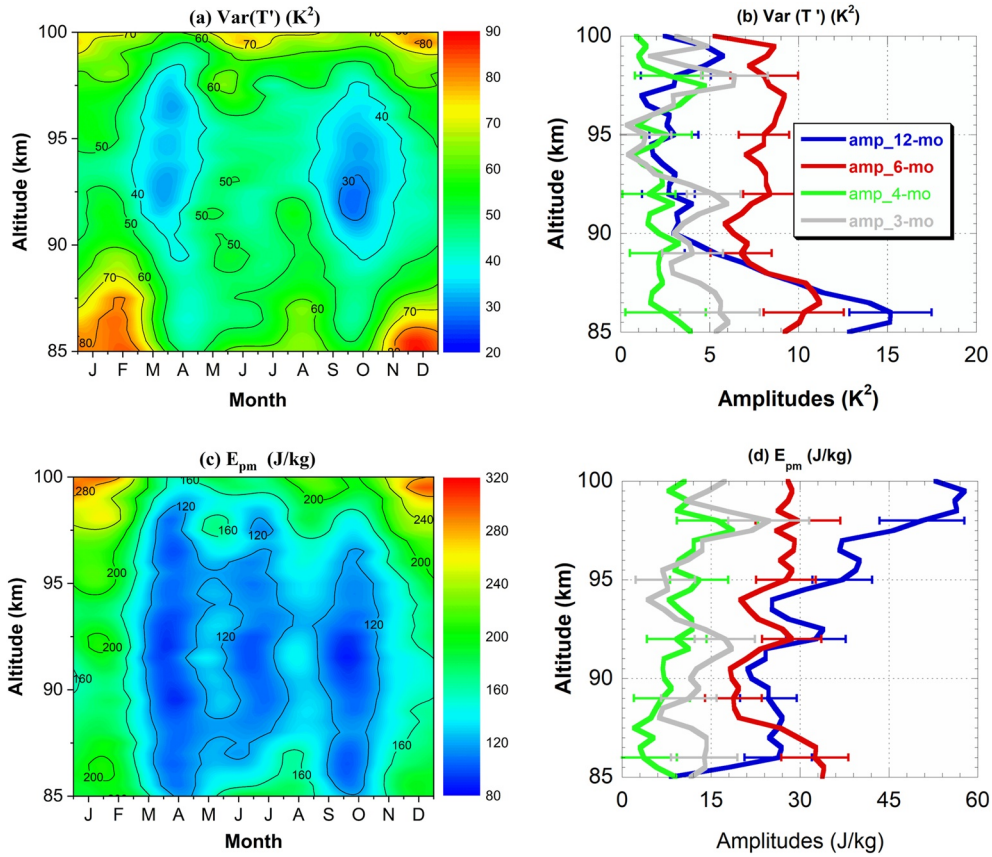

Figure 4. Month-altitude contours (left panels) and seasonal harmonic amplitude profiles (right panels): (a) and (b) for $Var(T')$, and (c) and (d) for E_{pm}; color code same as Figure 1b. See text for discussion.

SPR larger than AUT by ~20% below 90 km. The associated winter (WIN) and summer (SUM) profiles are not only different from those of the spring and autumn seasons but are also different between themselves. For $Var(T')$ as shown in Figure 5a, summer and winter are similar between 90 and 95 km; they start from about 50 K^2 at 90 km, decreasing to ~46 K^2 at ~ 95 km. Below 90 km, $Var(T')$ gradually increases to ~61 K^2 for summer and to ~83 K^2 for winter at 85 km. Above 95 km, $Var(T')$ gradually increases to ~73 K^2 for summer and to ~75 K^2 for winter at 100 km. Comparing $Var(T')$ at three selected altitudes, we have (66.1 ± 3.1, 61.5 ± 3.1, 61.5 ± 3.0, and 83.4 ± 3.8K^2) at 85 km for (SPR, SUM, AUT, and WIN) respectively, (37.3 ± 1.8, 47.3 ± 1.8, 34.4 ± 1.7, and 44.1 ± 1.8 K^2) at 93 km, and (65.1 ± 3.3, 72.6 ± 3.4, 69.1 ± 3.2, and 74.8 ± 3.4K^2) at 100 km. Correspondingly, the altitude dependence of the seasonal averaged E_{pm} are (156.0 ± 7.7, 176.2 ± 7.7, 145.6 ± 7.5, and 186.2 ± 7.8 J/kg) at 85 km for (SPR, SUM, AUT, and WIN) respectively, (125.4 ± 6.5, 120.2 ± 5.4, 115.2 ± 6.3, and 168.7 ± 6.6 J/kg) at 93 km, and (207.5 ± 12.0, 180.5 ± 12.2, 213.1 ± 11.6, and 278.6 ± 12.3 J/kg) at 100 km. Thus, E_{pm} starts from a high value at 85 km (likely breaking occurs below this altitude) dissipating to a minimum at about 93 km. After this point, like the annual mean, the wave's potential energy increases with height to a higher (much higher in WIN) value at 100 km. Interestingly, we note that the shape of the potential energy appears to be nearly the same (virtually parallel to one another) for four seasons. Unlike the winter profile of $Var(T')$, which is smaller at 100 km (by ~10%) compared to that at 85 km, the winter value of E_{pm} at 100 km is much higher (by ~50%) than that at 85 km.

Similar to $\overline{T}(z)$ and $N^2(z)$, the uncertainties in the seasonal mean profiles of $Var(T')$ and E_{pm} are quite small as shown in Figures 5a and 5b). Numerically, the 1σ-uncertainty of $Var(T')$ ranges from 4.4% to 5.4%, 3.8% to 5.9%, 4.6% to 5.4%, and 3.8% to 4.5% for spring, summer, autumn, and winter, respectively. For E_{pm}, the 1σ-uncertainty ranges from 4.7% to 6.0%, 4.4% to 7.1%, 4.9% to 5.8%, and 3.6% to 4.4%, respectively. These relatively small errors strengthen our confidence in the analysis. The credit here belongs to the large data set used (also

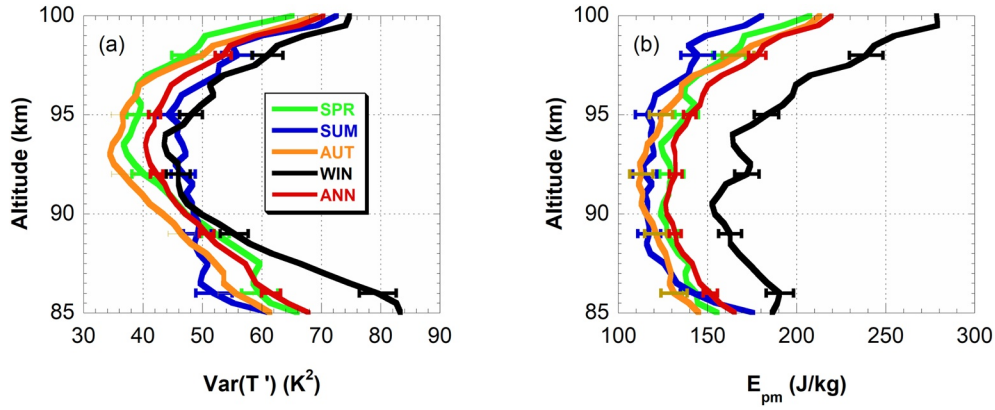

Figure 5. Annual and seasonal-mean profiles of (a). $Var(T')$ and (b). $E_{pm}(z)$, annual-mean in red and seasonal means, spring in green, summer in blue, autumn in brown, and winter in black, derived respectively from the data plotted in Figures 4a and 4c.

Table 1
Seasonal and Annual Means of Temperatures $\overline{T}(z)$ and Buoyancy Frequency Square $N^2(z)$

Quantity	Background temperature $\overline{T}$ (K)					Buoyancy freq. square $N^2(10^{-4}s^{-2})$				
Altitude (km)	Spring mean	Summer mean	Autumn mean	Winter mean	Annual mean	Spring mean	Summer mean	Autumn mean	Winter mean	Annual mean
105	191.7	202.6	192.8	183.4	192.7	6.4	5.6	6.2	6.0	6.0
104	188.4	201.0	190.0	181.5	190.3	6.2	5.9	6.0	5.5	5.9
103	185.3	197.6	186.8	180.5	187.6	5.9	6.0	5.9	5.2	5.7
102	183.5	194.7	184.7	180.7	185.9	5.4	5.8	5.6	4.7	5.4
101	182.7	192.7	183.6	181.4	185.1	4.6	5.5	4.7	4.1	5.0
100	182.9	191.0	183.5	182.3	185.0	4.6	5.5	4.7	4.1	4.7
99	183.8	189.6	184.2	184.5	185.5	4.3	5.4	4.4	3.8	4.5
98	185.2	188.4	185.5	186.8	186.5	4.1	5.3	4.1	3.6	4.3
97	186.9	187.4	187.2	189.3	187.7	3.7	5.1	3.8	3.3	4.1
96	189.0	186.7	189.1	192.1	189.2	3.7	5.1	3.8	3.3	4.0
95	191.2	186.4	191.2	195.0	191.0	3.7	5.1	3.7	3.2	3.9
94	193.2	185.9	193.2	197.9	192.5	3.7	5.1	3.7	3.2	3.9
93	195.1	185.3	195.1	200.9	194.1	3.8	5.2	3.7	3.1	4.0
92	196.8	184.6	196.9	203.9	195.5	3.9	5.4	3.9	3.1	4.1
91	198.0	183.4	198.2	206.2	196.6	4.2	5.6	4.1	3.3	4.3
90	198.4	182.0	199.0	208.5	197.0	4.5	5.7	4.3	3.6	4.5
89	198.2	181.2	199.1	209.3	197.0	4.7	5.8	4.5	3.7	4.7
88	197.8	178.9	199.2	211.4	196.8	4.9	5.9	4.7	3.9	4.8
87	196.8	177.4	198.8	212.0	196.2	4.9	5.7	4.8	4.1	4.9
86	196.5	176.5	198.0	212.2	195.8	4.9	5.5	5.0	4.3	4.9
85	195.8	175.9	197.0	211.9	195.1	5.0	5.3	5.1	4.6	5.0
84	195.3	176.0	196.1	210.9	194.5	5.0	5.2	5.2	5.0	5.1
83	194.3	176.0	194.9	208.9	193.5	5.5	5.8	6.0	6.0	5.8
Mean	**191.6**	**186.1**	**192.4**	**197.0**	**191.8**	**4.7**	**5.5**	**4.7**	**4.1**	**4.8**

Table 2
Seasonal and Annual Means of Var(T′)(z) and Potential Energy $E_{pm}(z)$

Quantity	Variance of wave perturbation $T'(K^2)$					Unit mass potential energy $E_{pm}(J/kg)$				
Altitude (km)	Spring mean	Summer mean	Autumn mean	Winter mean	Annual mean	Spring mean	Summer mean	Autumn mean	Winter mean	Annual mean
100	65.1	72.6	69.1	74.8	70.4	207.5	180.5	213.1	278.6	219.7
99	50.5	60.0	58.1	76.1	58.9	170.9	149.2	190.4	255.1	191.2
98	47.4	55.9	50.0	61.0	53.5	163.0	144.5	167.3	239.1	178.4
97	40.9	52.6	42.0	53.5	47.1	144.3	139.2	142.7	207.8	158.2
96	38.6	46.5	38.9	51.9	43.9	137.0	120.8	135.0	197.7	147.3
95	39.2	44.3	36.5	48.1	41.9	138.5	116.4	124.0	183.2	140.2
94	37.9	45.7	36.1	43.8	40.8	129.3	118.0	121.4	164.0	132.9
93	37.3	47.3	34.4	44.1	40.7	125.4	120.2	115.2	168.7	132.1
92	40.1	46.8	36.7	45.9	42.3	130.1	114.9	113.0	172.3	132.2
91	44.3	47.3	39.8	46.4	44.4	128.4	115.1	113.8	156.7	128.3
90	47.1	48.4	43.3	49.7	47.1	123.7	115.8	115.7	154.2	127.1
89	52.2	49.1	46.5	55.4	50.7	127.3	117.4	121.1	162.8	131.9
88	57.3	49.4	50.6	61.7	54.7	133.9	118.1	126.4	167.5	136.3
87	58.8	50.0	53.6	70.3	58.1	137.5	129.5	129.7	178.2	143.5
86	59.7	52.0	55.6	79.5	61.6	143.6	142.4	131.4	190.7	151.7
85	66.1	61.5	61.5	83.4	68.0	156.0	176.2	145.7	186.2	165.7
Mean	**48.9**	**51.8**	**47.0**	**59.1**	**51.5**	**143.5**	**132.4**	**137.9**	**191.4**	**151.0**

see discussions in Appendix B), permitting accurate harmonic fitting. The climatological seasonal averages of $Var(T')$ and E_{pm} are tabulated at 1-km interval in Table 2.

5. Discussion

Our harmonic analysis using $F(t)$ in Equation 2 consists of a constant and sinusoidal variations with periods of 12-month, 6-month, 4-month, and 3-month at each altitude. Due to the large total number of well-distributed observations over many years, most of the DOY have at least one night of observation, though with nonuniformly spaced observation times each year. Therefore, the sinusoidal components in the fit function are nearly orthogonal to one another. Indeed, with same data points, the resulting constant and amplitudes and phases of the 12-month and 6-month periods remain essentially the same should we remove the 4-month and 3-month sinusoidal terms from Equation 2. The 4-month and 3-month harmonics are smaller by roughly a factor of 2 or more compared to the 12-month and 6-month periods in $Var(T')$ and $E_{pm}(z)$, and much smaller in $\overline{T}(z)$ and $N^2(z)$. With 956 nights of data acquired over 20 years, we can describe the two-level midlatitude (e.g., at 40.6°N) mesopause temperature with clarity and precision. There exists an altitude of maximum temperature variation of $\Delta T = 42.9$K at 85.5 km and an altitude of minimum temperature variation of $\Delta T = 9.5$K at 98 km. The associated annual amplitudes are respectively 19.5 ± 0.5K and 0.7 ± 0.4K. These extremal amplitudes may be compared to the night portion of the 2-year midlatitude diurnal-cycle observations at Urbana, IL (40°N, 88°W) and CSU (40.6°N, 105°W) in late 1990s yielded results closer to our results presented here. The former observation showed ∼1.0K at ∼98 km and ∼14K at ∼85 km in Figure 4 of States and Gardner (2000) and the latter showed ∼5K at ∼98 km and ∼24K at 86 km in Figure 4c of Chen et al. (2000) for minimum and maximum amplitudes, respectively. They can also be compared to those of a higher-latitude site, Kühlungsborn (54°N) with maximum amplitude of 28K at 85 km and minimum amplitude of 3K at 102 km (Gerding et al., 2008). Since the two-level mesopause exists in both hemispheres, the extrema altitudes and amplitudes also exist in the Antarctic sites, South Pole (Pan & Gardner, 2003) and Syowa Station (Kawahara et al., 2004). The former observes a minimum annual variation of ∼3K at 99 km and max annual variation of ∼32K at 85 km, while the latter observes min annual variation of ∼5K at 98 km and max variation of ∼30K at 84 km. We tabulate the altitudes and temperatures of max and min annual amplitudes of

Table 3
Summary of Annual (12 months) Temperature Variations in the Mesopause Region

Site	References	Low-altitude maximum		High-altitude minimum	
		Altitude	12-month amplitude	Altitude	12-month amplitude
S Pole (90°S)	Pan and Gardner (2003)	85 km	32K	99 km	3.0K
Syowa (69°S)	Kawahara and Gardner (2004)	84 km	30K	98 km	5.0K
Kühlungsborn (54°N)	Gerding et al. (2008)	85 km	28K	102 km	3.0K
CSU (40.6°N)	This paper	85.5 km	20K	98 km	1.0K
Urbana (40°N)	States and Gardner (2000)	85 km	14K	97.5 km	1.0K
Starfire (35°N)	Chu et al. (2005)	87 km	15K	96.5 km	1.0K
Maui (20.7 N)	Chu et al. (2005)	86 km	9.5K	97 km	3.5K

these stations along with those of SOR (35°N) and Maui (20.7°N) taken from Chu et al. (2005) in Table 3 for easy comparison. We note that the low-altitude max amplitude generally increases with increasing (absolute) latitude, while the high-altitude min amplitude is relatively constant.

The mesopause altitude exhibits bistable behavior with high winter mesopause varying between 98 and 103 km and the low summer mesopause at 84 ± 1 km with sharp transitions, giving rise to a 102-day summer season between 121 and 222 days of the Year. We can determine the sharp transitions to such a precision because there is no data gap through the transition periods. In fact, there are more than 10 nights of continuous data centered on either transition in this data set. Though not emphasized at the time, we can see the sharpness in transitions between winter/summer mesopause altitudes clearly in the temperature contour plot based on the 8-year data set without invoking on the best fit to seasonal harmonics, Figure 3a of She et al. (2000). The advantage of using the best fit harmonic analysis for mesopause altitude study was previously demonstrated by States and Gardner (2000), Chu et al. (2005), and Gerding et al. (2008). They were able to reveal sharp mesopause transitions respectively in Figures 6a, 12, and 8 of the respective publications with only 52 weekly sets of data over Urbana, IL (40°N), 58 nights and 266 nights of well distributed data. According to She and von Zahn (1998), the bistable mesopause altitude with longer winter state exists with roughly 4-month in the summer state (later determined to be about 120 days, see Gerding et al., 2008) at 54°N, and as it is determined here to be 102 days for the summer state at midlatitude at 40.6°N. In the equatorial region, only high winter mesopause exists (von Zahn & Höffner, 1996), resulting from radiative thermal balance, as the residual meridional flow (from summer pole to winter pole) exerts neither cooling nor warming in the equatorial region. Indeed, the nocturnal temperature climatology based on 106 nights of K lidar observations at Arecibo Observatory, Puerto Rico (18.35°N, 66.75°W), Figure 6b of Friedman and Chu (2007), reveals an SAO thermal structure.

With 20 years of data over the same site, the data set is also poised for an assessment of interannual variability of the two-level mesopause, such as the length of the short/summer mesopause. Since the data set consists of only ∼50 nights per year, one may need to group several years of data together for such analysis. It is also of interest to investigate the solar flux/cycle dependence of the two-level mesopause in the future.

The seasonal variation of GW activities, either in terms of waves' variance or potential energy, often is reported in terms of a scatter plot over a year span. From such a plot, an author typically concludes by inspection that the wave activities are either AO dominance (winter max and summer min) or SAO dominance (major peak in winter and minor peak in summer with spring and autumn minima in between). Although other models exist, the annual variations/oscillations (AOs) of GWs observed in midlatitude and polar region in stratosphere and low mesosphere is usually explained with the selective filtering of GWs by the difference of prevailing winds between summer and winter. The SAO dominance of GWs in tropic upper stratosphere and lower mesosphere may be explained by selective filtering by the lower stratospheric SAO wind (Li et al., 2010). That SAO in GWs in the middle mesosphere, also observed in radar wind variances at 35°S, 35°N, and 52°N (Nakamura et al., 1996) as well as in lidar temperatures (Mze et al., 2014; Wilson et al., 1991), still beg for a good explanation. Some of these discrepancies may result from the difference in temporal resolution employed. For example, at 44°N, initial OHP observations were analyzed at 26 min resolution (Wilson et al., 1991), later at 15 min resolution (Mze et al., 2014), and those of Toronto observations at 30 min resolution (Whiteway & Carswell, 1995). The radar

observations at 35°S, 35°N, and 52°N were analyzed at 5 min resolution, while the MLO lidar at 19.5°N had 30 min resolution. Furthermore, wind filtering is more complex than commonly believed as most studies ignore the possible generation of secondary waves (Van Zandt & Fritts, 1989). Recent studies (Vadas & Becker, 2019) showed when the primary wave breaks, secondary waves could be generated, implicating that the presence of a critical layer does not always prevent wave energy from propagating upwards.

The truth is of course both annual and semiannual variations exist in any data set. Thus, for observations with sufficient data and good signal-to-noise, it is better to present the amplitudes and phases of both AO and SAO components and compare them directly. Indeed, this is also the manner in the midlatitude mesopause region GW activities observed at SOR were analyzed. Comparing the annual mean of SOR $Var(T')$, black curve in Figure 5b of Gardner and Liu (2007) to the red curve in Figure 5a of CSU observation reported here, we found that the annual mean profiles between 95 and 100 km are comparable, both increasing from ∼40 K^2 to ∼70 K^2, while the CSU result decreases monotonically from 68 K^2 at 85 km to ∼41 K^2 at 93 km, but the SOR result increases from 85 to 90 km and then decrease until 95 km. Both showed stronger semiannual amplitude compared to annual amplitude between 88 and 100 km with SOR results in Figure 5b of Gardner and Liu (2007) about a factor of 2 larger than CSU results shown in Figure 4b here. The larger semiannual amplitudes between 88 and 100 km in Figure 5b is consistent with the larger summer values of $Var(T')$, shown in blue in Figure 5a, than spring (in green) and autumn (in orange) values by about ∼10 K^2 in the same altitude range. Although SOR and CSU are both mid-latitude mountain sites, the topography and climate conditions are considerably different, which means the GW sources will differ. For example, SOR, which is located about 625 km south of CSU, is sited at the western base of the Manzano Mountains which form a single north/south ridge of mountains rising about 1.5 km above the Rio Grande River Valley. The topography to the west is high plateau with some lower-lying mountains extending into Arizona. CSU is located at the eastern base of the front range of the broad Rocky Mountain Range, which rises to 2.75 km above Ft. Collins, with high prairie to the east. Because of the prevailing eastward winds, the CSU mesopause is affected more by mountain waves than SOR. Thus, it is not surprising that the vertical profiles of $Var(T')$ are different at these two sites (see companion paper, Gardner et al., 2022). The strong semi-annual variation in $Var(T')$ observed at SOR, in contrast to the strong annual variation observed at CSU, is likely a consequence of differences in weather and data sampling biases related to climate. Convective activity associated with the summer monsoon is stronger at the more southerly SOR site. Furthermore, the SOR observations were conducted from June 1998 to November 2000, before the current southwest mega-drought (Williams et al., 2022). The CSU observations were conducted from March 1990 to 2010. About half the CSU observations were acquired before the onset of the drought and half during the drought. Thus, the summer convective gravity activity represented by the CSU data set, is expected to be considerably attenuated compared to the SOR data set.

Due mainly to more stable background temperatures in summer months (larger N^2 values), the entire profile of summer potential energy $E_{pm}(z)$ become comparable to those profiles in spring and autumn, see Figure 5b. There have been two reports on GW potential energy measurements between 85 and 100 km. One is by Rauthe et al. (2008) at midlatitude (54°N), and the other is from Yue et al. (2018) at an equatorial region (18.4°N). Our seasonal profile of $E_{pm}(z)$ in Figure 5b is consistent in shape and magnitude with Figure 7 of Rauthe et al. (2008), even though they presented potential energy per unit volume $E_{pv}(z)$. A spot check of our E_{pm} at 86 km, see Table 2 with E_{pm} = 143.6, 142.4, 131.4, and 190.7 J/kg for SPR, SUM, AUT, and WIN, respectively, is in order. Using the 1976 standard air density at 86 km of 6.96×10^{-6} kg/m^3, our E_{pv}(86 km) are 0.999, 0.991, 0.915, and 1.327 mJ/m^3, respectively, consistent with theirs. Although our contour plot, Figure 4c is not expected to be like that at an equatorial region, Figure 4a of Yue et al. (2018), the shapes of the annual mean profile apparently are similar, comparing our red curve in Figure 5b to the solid curve in their Figure 4c. We note with interest that their annual means are larger than ours by 2–4 times.

In a recent study, She et al. (2019) invoked GW activities to qualitatively account for the difference between summer and winter temperature trends. Their arguments depend upon the GWs trend studies from radar zonal wind data by Jacobi (2014) and from SABER temperature data by Liu et al. (2017), both implicating negative 4-month summer trend and positive 6-month winter trend between 85 and 95 km. With the 20-year observation of lidar temperatures and GW $E_{pm}(z)$ time series at the same location on hand, we can in principle consider the influence of GW activities on the long-term temperature trend directly. Unfortunately, unlike in the 28 years of lidar nightly temperatures, which show visible linear trend and solar cycle response in the scatter plots, see Figure

2 of She et al. (2019), there exists no consistent linear trend in the scatter plots of the 20 years of GW $E_{pm}(z)$. We thus cannot report any consistent trend of GWs potential energy in this data set (1990–2010).

6. Conclusion

In conclusion, using a total of 956 nights (4–14 hr, each night, a total of ~7,000 hr) of Na lidar temperature observations, we deduced nightly mean temperature profiles, from which we presented the climatology of a midlatitude two-level mesopause temperature structure with clarity and precision. The mesopause altitude may be divided into a long season (winter, much higher altitude) and a short season (summer, of 102 days at 40.6°N) with sharp transitions between them. The same data set, when analyzed in 10-min and 1-km resolution allowed us to deduce the seasonal variation of GW activities for vertical wavelengths between 3 and 15 km, see appendix A of Gardner et al. (2022). Seasonal averages of $Var(T')$ and $E_{pm}(z)$ were made for four seasons, spring, summer, autumn, and winter, with 236, 229, 274, and 217 nights of data, respectively. We found all profiles starting from a value at 85 km decreasing to a minimum at 90–93 km and then increasing exponentially to a larger value at 100 km, suggesting waves in the mesopause region generally (or climatologically) break below 85 km and begin dissipating energy against a background with decreasing density that exponentially increases the wave amplitude. The two forcings balance each other at the amplitude minimum at 90–93 km, after which the amplitudes grow again with altitude. The uncertainties for both $Var(T')$ and $E_{pm}(z)$ are about 4% for winter and about 5% for other three seasons. Inspection of Figure 5a and the associated values at 93 km, we see a clear semiannual variation in $Var(T')$, while inspection of Figure 5b and associated values at 93 km, we see a clear annual variation in E_{pm} with winter value about 40% higher than other three seasons. The E_{pm} profiles of SPR, SUM, and AUT are similar; their average profile (not shown) starts from a value of 153.3 J/kg at 85 km reaching the minimum of ~119 J/kg around 93 km, and then increasing to 200.4 J/kg at 100 km; in comparison, the winter minimum of 154.6 J/kg at 90–91 km is ~30% higher than the minimum of the three season mean. Without considering secondary waves, generated in the lower atmosphere, atmospheric waves are filtered by the prevailing wind system, which is eastward in the troposphere in both winter and summer, and eastward in winter and westward in summer in the stratosphere and lower mesosphere. Thus, topographic (strong) and westward GWs in winter, and only high-speed eastward GWs in summer are allowed to propagate into the MLT. This leads to the division of associated potential energy into a long season (SPR + SUM + AUT) and a short season (winter, higher potential energy). Unlike the background temperature, the transitions between long and short seasons of GWs are more gradual. These filtered upward propagating GWs experience dissipation. To balance the dissipating momentum, Coriolis forces are enacted on the background atmosphere in both hemispheres. Together, they create a meridional flow (from summer pole to winter pole) globally in the MLT that leads to the creation of the low summer mesopause in polar regions and midlatitudes with sharp transitions. Our study on the climatology of both background temperature and GW potential energy based on the same 20-year-long (956 nights of observation) data set clearly and firmly supports our current understanding of the coordinated local (within the hemisphere) and global (across hemispheres) effects of atmospheric GWs in the MLT.

Appendix A: Derivation of Wave Perturbations and Related Functions

To deduce the nightly mean variance of wave perturbations $Var(T'(z)) = <(T'(z))^2>$ and associated photon noise uncertainty $<(\delta T(z))^2>$ from the high-resolution temperature profiles $T(z,t_i) \equiv T_i(z)$ at each interval t_i, we follow the procedures of Gardner and Liu (2007). Depending on season and weather, the duration of nocturnal observations ranges from 4 to 14 hr. The number of available time interval depends on the length of observation; for example, $i = 1,2,3,\ldots$, 60 for a 10 hr night. We first compute sample temperature perturbations $T^s(z,t_i) \equiv T_i^s(z)$ and uncertainties $\delta T^s(z,t_i) \equiv \delta T_i^s(z)$ from the measured temperatures, $T(z,t_i) \equiv T_i(z)$, and associated uncertainties $\delta T(z,t_i) \equiv \delta T_i(z)$ at each altitude z and time interval t_i, from which we derive nightly mean sample $Var(T^s)$ for each altitude z by subtracting nightly linear background from the observed temperatures; the resulting temperature perturbations that exceeded three standard deviations from the nightly mean were considered as occasional outliers and removed. This quality control procedure is followed by vertical-mean (between 85 and 100 km) removal for each time interval t_i, resulting in sample perturbation $T_i^s(z)$. Using the resulting $T_i^s(z)$ and associated uncertainties, $\delta T^s{}_i(z) \approx \delta T_i(z)$, where $\delta T_i(z)$ is the measured uncertainty due to photon noise as the uncertainties due to linear background subtraction and vertical-mean removal are much smaller in comparison. We then calculate nightly mean $Var(T^s(z))$ and associated uncertainty.

As an example, we deduce the linear background subtracted (LBS) temperature profiles $T_i^{LBS}(z)$ from the 72 temperature profiles $T_i(z)$, that is, i = 1,2,3,…..72, observed in the 12-hr duration in the 338th night in 2006. For this long data set in a winter night, the Na layer extended beyond 80 and 105 km, and, within this altitude range, the quality control procedure finds no outlier. Since the CSU data excludes temperature data with $\delta T_i(z) > 10\ K$, outliers rarely exist between 85 and 100 km for nocturnal temperatures, as noticed previously by Acott et al. (2010), and we use the same notation $T_i^{LBS}(z)$ for the profiles after the quality control procedure. After the vertical-mean (between 85 and 100 km) is removed from $T_i^{LBS}(z)$, we have the final sample perturbation temperatures $T_i^s(z)$. These profiles and time-altitude contour plots are shown respectively in Figure A1: (a) and (b) for $T_i(z)$, (c) and (d) for $T_i^{LBS}(z)$, and (e) and (f) for $T_i^s(z)$.

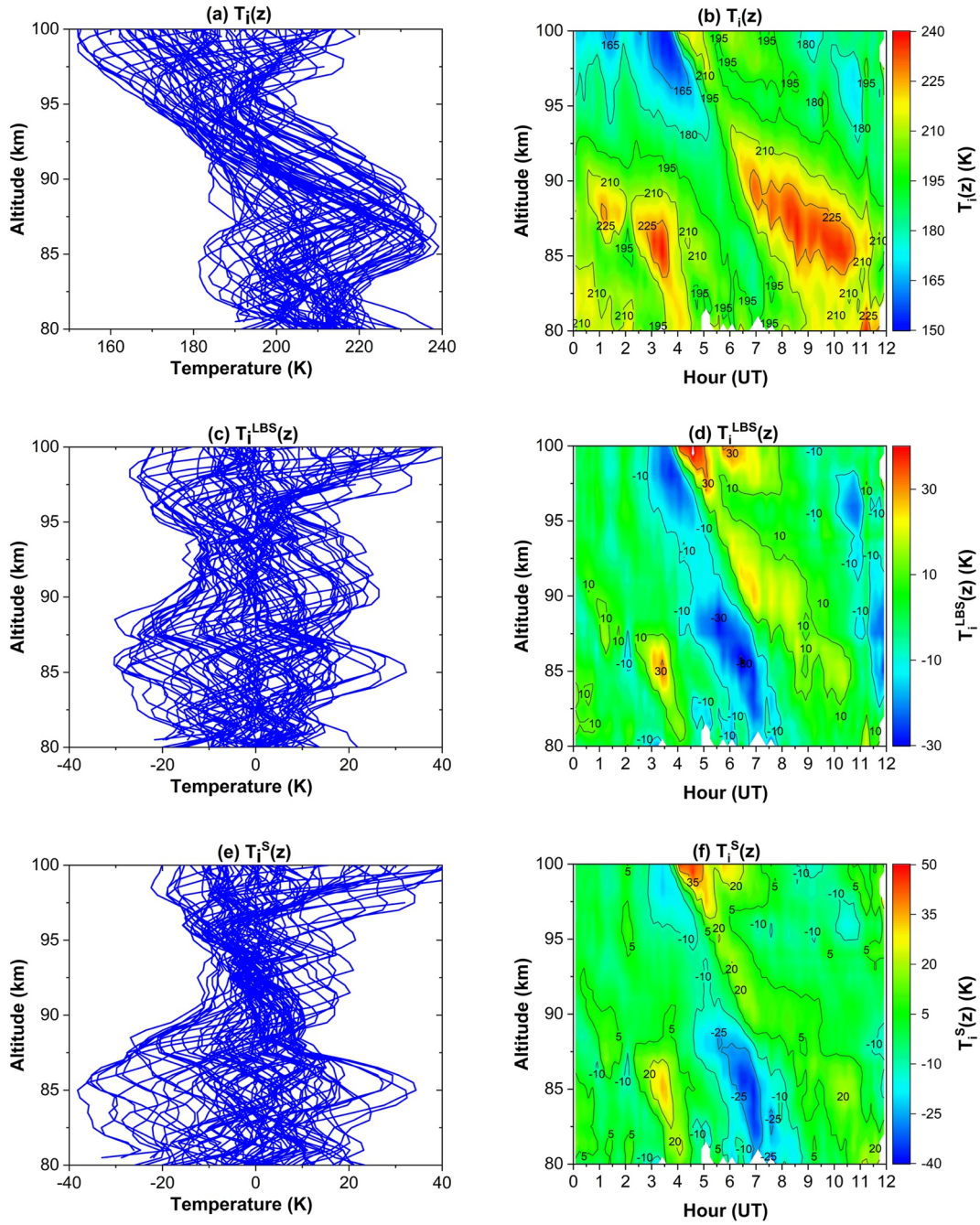

Figure A1. Sequential deduction of temperature (or perturbation) profiles and their time-altitude contours plots from one night's (the night of 338 in 2006) observation. Temperatures in 10-min interval $T_i(z)$, (a) and (b), linear background subtracted perturbations $T_i^{LBS}(z)$, (c) and (d), and sampled wave perturbations of $T_i^s(z)$ after vertical mean removal, (e) and (f).

A deduced sample temperature perturbation profile $T_i^s(z)$ is the sum of wave-induced perturbations $T_i'(z)$and photon noise uncertainty $\delta T^s{}_i(z)$, with $|\delta T^s{}_i(z)| \approx \delta T_i(z) \geq 0$, the latter is a random variable with zero mean, that is, $T_i^s(z) = T'{}_i(z) \pm \delta T_i(z)$ with $\langle \delta T(z) \rangle = 0$. Since $T'{}_i(z)$ and $\delta T_i(z)$ are independent, the ensemble average (simple average) and variance of wave perturbations $T_i'(z)$ may be derived as:

$$
\begin{aligned}
&< T'(z) >= \overline{T'}(z) = \frac{1}{n}\sum_{i=1}^{n} T_i'(z) = 0; < T^s(z) >= \overline{T^s}(z) = \frac{1}{n}\sum_{i=1}^{n} T_i^s(z) = 0, thus,\\
&Var\,(T^s(z)) =< (T^s(z))^2 >=< (T'(z) \pm \delta T(z))^2 >=< (T'(z))^2 > + < (\delta T(z))^2 >, or \qquad \text{(A1)}\\
&\overline{(T'(z))^2} = \overline{(T^s(z))^2} - \overline{(\delta T(z))^2}; \overline{(T^s(z))^2} = \frac{1}{n}\sum_{i=1}^{n} \left(T_i^s(z)\right)^2; \overline{(\delta T(z))^2} = \frac{1}{n}\sum_{i=1}^{n} (\delta T_i(z))^2
\end{aligned}
$$

Here, we assume the time averages (over bars) are equal to the ensemble average (angle brackets). The last expression, Equation A1, suggests that the variance of the temperature wave perturbation can be deduced from the difference between the variance of sample temperature perturbations and that of noise perturbations, both measured from observation data. The noise perturbation $\delta T(z)$ can make the sample variance $<(T^s(z))^2>$ either bigger or smaller than the variance of the wave perturbation $<(T'(z))^2>$ it represents. When the wave perturbation $<(T'(z))^2>$ computed from Equation A1 is negative, it is not acceptable, and we consider this nightly mean variance an outlier. The same noise perturbations can also make $<(T^s(z))^2>$ larger than $<(T'(z))^2>$ really is. To remove these unwarranted influences (or outliers), we believe it is also justifiable to reject at each altitude the same number of noise-contaminated largest nightly mean variances as those giving negative variances. The number of outliers rejected by this additional quality control will be small near the peak of the Na layer and increases toward the edges of the Na layer. Shown in Figure A2a are plots of the percentage of rejected noise-contaminated nightly mean $Var(T')$ that are either negative (black solid) or too large (open red) between 80 and 105 km. Notice that the total rejections are less than 2% near the layer peak (~91 km). At the edges of the altitude range of interest (85–100 km), total rejections are ~5% at 85 km at the lower edge, and at the upper edge are ~20% at 100 km, even here we still have 765 nights of good data. The same procedure will be applied to determine the outliers in the variances of the gradient perturbations $Var(dT'(z)/dz) = <(dT'(z)/dz)^2>$ to be used in the companion paper (Gardner et al., 2022). For a moderate lidar like the CSU Na lidar with power-aperture product of ~0.05 W m^2, this additional quality control procedure is necessary for $z > 95$ km. Indeed, an earlier paper (Acott et al., 2010) using high-resolution data between September 2006 and August 2007, the authors reported GW variances and zonal momentum fluxes only between 85 and 95 km.

Since the vertical range of measurements for wave activities is between 85 and 100 km and the vertical resolution is 1 km, the range of wavelengths included in our analysis is ideally between 2 and 15 km. For the 10-min integrated data set, the shortest wave period we include in the analysis is 20 min. The combined impact of the Hanning window (2 km full width) and the temporal integration of 10 min yields a 3-dB cutoff wavelength of about 3 km, see appendix A of Gardner et al. (2022), thus our analysis includes waves with vertical wavelengths

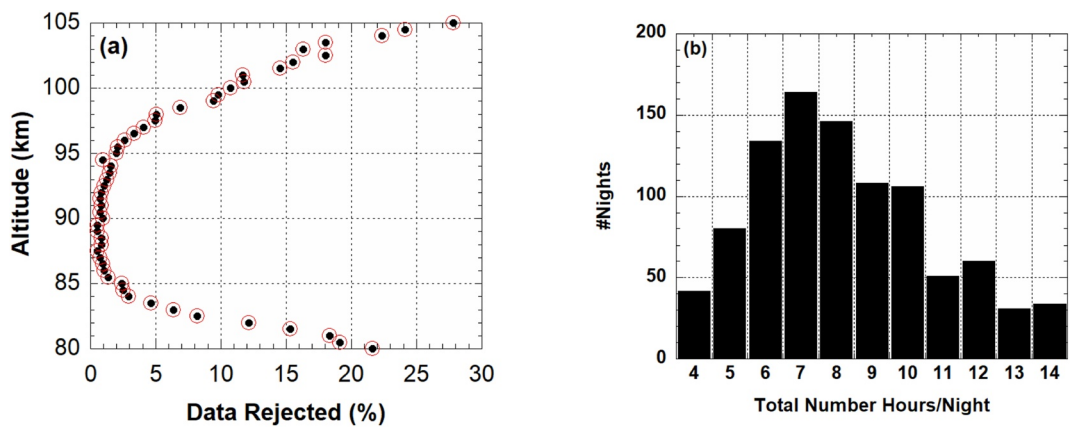

Figure A2. (a) Percentage of data points rejected owing to photon noise contamination between 80 and 105 km, making the resulting $Var(T')$ either negative (solid black circle) or too large (open red circles). (b) The distribution of number of nights (totaling 956 nights) as a function of number of hours per night; the average is 8.2 ± 2.5 hr.

ranging from 3 to 15 km. Depending on the data length each night, the longest wave period covered ranges from 4 to 14 hr. For example, a 9-hr night, our analysis includes both GWs and the terdiurnal tide, while for a night with 13-hr or 14-hr observation, the semidiurnal tide is also included in the analysis. Figure A2b gives the distribution of observed nightly mean background temperatures versus hours with observation per night, yielding an average data length of 8.2 ± 2.5 hr per night.

Gardner and Chu (2020) recently advocate the collection of lidar photon files with short integration times, in seconds for example, With such a data set, one can calculate variance of $T_i^s(z)$ by the covariance of the neighboring samples. Since the neighboring noise perturbations, $\delta T_i(z)$ and $\delta T_{i+1}(z)$ are uncorrelated, the covariance of the neighboring samples equals to the variance of the wave perturbations. In such a system, no additional quality control would be needed.

A companion paper (Gardner et al., 2022) addresses, in addition to $\overline{T}$, N2, and $Var(T')$, the variance of temperature gradient perturbations, $dT'_i(z)/dz$, which are deduced as:

$$\left\langle \left(\frac{dT'}{dz} \right)^2 \right\rangle = \frac{\left\langle (T'_2 - T'_1)^2 \right\rangle}{(z_2 - z_1)^2} = \frac{\left\langle (T'_2)^2 \right\rangle - 2\left\langle T'_2 T'_1 \right\rangle + \left\langle (T'_1)^2 \right\rangle}{(z_2 - z_1)^2} \tag{A2}$$

where the variance and covariance are calculated from the sample perturbations as $\langle T_2{}' T_1{}' \rangle = \langle T_2{}^s T_1{}^s \rangle$ and $\langle (T'_{1,2})^2 \rangle = \langle (T^s_{1,2})^2 \rangle - \langle (\delta T_{1,2})^2 \rangle$. Due to vertical resolution of 1 km, the raw photon files are smoothed with a Hanning window of 2 km full width, we compute vertical gradient at z with $T_2(z_i + 1\ \text{km})$ and $T_1(z_i - 1\ \text{km})$ and $z_2 - z_1 = 2$ km, so that the respective photon noise-induced perturbations are uncorrelated. In the companion paper (Gardner et al., 2022), we also need quantities $\Gamma^2(z) = (d\overline{T}/dz + \Gamma d)^2$, normalized wave variance $\overline{\varsigma^2}$ (vertical displacement of an air parcel from equilibrium), and normalized gradient variance (or instability parameter) ξ_{inst}; they are defined as:

$$\overline{\varsigma^2} = \frac{Var(T')}{\left(\Gamma_d + d\overline{T}/dz\right)^2} \left(\text{in km}^2\right) = \left(\frac{g}{N^2}\right)^2 \frac{Var(T')}{\overline{T}^2} \text{ and } \xi_{inst} = \frac{Var(dT'/dz)}{\left(\Gamma_d + d\overline{T}/dz\right)^2} \tag{A3}$$

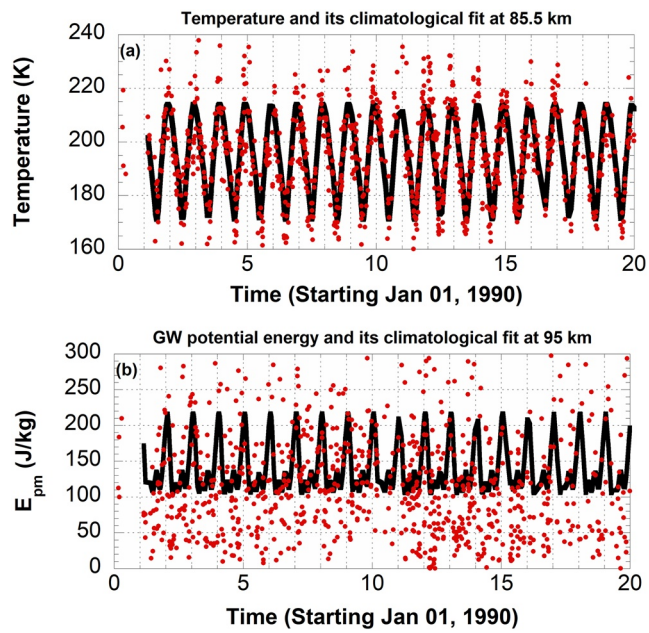

Figure A3. The 20-year time series of background temperature $\overline{T}$(K) at 85.5 km, and gravity wave potential energy $E_{pm}(J/kg)$ at 95 km in red dots are plotted with the associated climatological fit in black curves, respectively in (a) and (b).

Appendix B: The Goodness of Climatological Fits and the Merit of a Long Data Set

To examine the variability of the data points from the climatological best fits, we plot the nightly temperature (red dots) at 85.5 km and wave potential energy E_{pm} (red dots) at 95 km as a function of day with the associated climatological best fits (black curves), respectively in Figures A3a and A3b. In Figure A3a, not only the temperature climatology fit appears to well represent the data points with small scatters, the goodness of the fit is also comparable from one year to the next, suggesting that the climatological seasonal harmonics and seasonal averages of temperature presented in Figures 1a, 1b, and 3a may be obtained with 1 or 2 years of well-distributed data of about 50 nights per year. This however is not the case when it comes to functions of temperature perturbations, like E_{pm}. With a careful examination, we can see more high value points occur more-or-less in winter near the vertical grid lines in Figure A3b, and low value points likely fall between the grid lines near the minima of the fit; however, the scatters are displeasingly large. In addition, the goodness of the fit appears to be different from one year to the next. Therefore, the reason the uncertainties in the climatological seasonal harmonics and seasonal averages presented in Figures 4c, 4d, and 5b are small is because they are the result of linear regression fit with 20 years and 956 nights of well-distributed observation of GW perturbations. Using one or 2 years of data, the climatology best fit and associated seasonal means may look noticeably different. Indeed, we had compared (not shown here) Figure 5b, the four seasonal means deduced from the climatological fit, to the four seasonal means evaluated directly from one year (2003), 5 years (2001–2005), 10 years (1995–2004), and 20 years (all) of data. We found with 1 year of data only winter results between 86 and 95 km resembles that shown in Figure 5b. If we use 5 years of data, all four seasons between 86 and 95 km are like those in Figure 5b. With 10 years of data, all four seasons between 86 and 99 km are similar, and with 20 years of data, the straight four seasonal means appear to be identical to those shown in Figure 5b between 85 and 100 km. Thus, for a modest Na lidar like the CSU Na lidar, the availability of multiple years of data is essential for a reliable climatological fit for GW activities and the application of the additional quality control is necessary to extend the altitude range of validity from 95 to 100 km.

Data Availability Statement

The nightly mean and high-resolution CSU Na lidar temperature data (1990–2010) are available respectively from Madrigal Database at Millstone Hill and from Digitalcommons of Utah State University. Use of the Madrigal Database (http://millstonehill.haystack.mit.edu/) is generally subject to the NSF/CEDAR Rules-of-the-Road; prior permission to access the data is not required. The data at Digitalcommons is a part of the open access USU-CSUs Lidar Data (https://digitalcommons.usu.edu/all_datasets/54/). Both data sets can be downloaded with a simple procedure in text format.

Acknowledgments
This study was supported in part by the Strategic Priority Research Program of Chinese Academy of Sciences (Grant XDA17010303) and by NSF Grant AGS-2029162. The lead author acknowledges with great appreciation the contribution of all former students and visitors who participated in data acquisition at the CSU Na lidar site.

References

Acott, P. E., She, C.-Y., Krueger, D. A., Yan, Z.-A., Yuan, T., Yue, J., & Harrell, S. (2010). Observed nocturnal gravity wave variances and zonal momentum flux in mid-latitude mesopause region over Fort Collins, Colorado, USA. *Journal of Atmospheric and Solar-Terrestrial Physics*, *74*(4), 449–456. https://doi.org/10.1016/j.jastp.2010.10.016

Chen, S. S., Hu, Z. L., White, M. A., Krueger, D. A., & She, C. Y. (2000). Lidar observations of seasonal variation of diurnal mean temperature in the mesopause region over Fort Collins, CO (41oN, 105oW). *Journal of Geophysical Research*, *105*, 12371–12379. https://doi.org/10.1029/2000jd900045

Chu, X., Gardner, C. S., & Franke, S. J. (2005). Nocturnal thermal structure of the mesosphere and lower thermosphere region at Maui, Hawaii (20.7oN), and Starfire Optical Range, New Mexico (35oN). *Journal of Geophysical Research*, *110*, D09S03. https://doi.org/10.1029/2004JD004891

Chu, X., Zhao, J., Lu, X., Harvey, V. L., Jones, R. M., Becker, E., et al. (2018). Lidar observations of stratospheric gravity waves from 2011 to 2015 at McMurdo (77.84°S, 166.69°E), Antarctica: 2. Potential energy densities, lognormal distributions, and seasonal variations. *Journal of Geophysical Research: Atmospheres*, *123*, 7910–7934. https://doi.org/10.1029/2017JD027386

Fricke, K. H., & von Zahn, U. (1985). Mesopause temperature derived from probing the hyperfine structure of the D2 resonance line of sodium by lidar. *Journal of Atmospheric and Terrestrial Physics*, *47*, 499–512. https://doi.org/10.1016/0021-9169(85)90116-3

Friedman, J. S., & Chu, X. (2007). Nocturnal temperature structure in the mesopause region over the Arecibo Observatory (18.35°N, 66.75°W): Seasonal variations. *Journal of Geophysical Research*, *112*, D14107. https://doi.org/10.1029/2006JD008220

Fritts, D. C., & Alexander, M. J. (2003). Gravity wave dynamics and effects in the middle atmosphere. *Reviews of Geophysics*, *41*(1), 1003. https://doi.org/10.1029/2001RG000106

Gardner, C. S., & Chu, X. (2020). Eliminating photon noise biases in the computation of second-order statistics of lidar temperature, wind, and species measurements. *Applied Optics*, *59*, 8259–8271. https://doi.org/10.1364/ao.400375

Gardner, C. S., & Liu, A. Z. (2007). Seasonal variations of the vertical fluxes of heat and horizontal momentum in the mesopause region at Starfire Optical Range, New Mexico. *Journal of Geophysical Research*, *112*, D09113. https://doi.org/10.1029/2005JD006179

Gardner, C. S., She, C.-Y., & Yan, Z.-A. (2022). *Seasonal variations of gravity wave induced thermal and constituent diffusivities in the mesopause region above Ft. Collins, CO (40.6°N, 105.1°W), a companion paper (submitted concurrently)*.

Gerding, M., Höffner, J., Lautenbach, J., Rauthe, M., & Lübken, F.-J. (2008). Seasonal variation of temperatures between 1 and 105 km altitude at 54 N by lidar. *Atmospheric Chemistry and Physics*, *8*, 7465–7482. http://www.atmos-chem-phys.net/8/7465/2008/

Guo, Y., & Liu, A. Z. (2021). Seasonal variation of vertical heat and energy fluxes due to dissipating gravity waves in the mesopause region over the Andes. *Journal of Geophysical Research: Atmospheres*, *126*, e2020JD033825. https://doi.org/10.1029/2020JD033825

Hitchman, M. H., Gille, J. C., Rodgers, C. D., & Brasseur, G. (1989). The separated polar winter stratopause: A gravity wave driven climatological feature. *Journal of the Atmospheric Sciences*, *46*, 410–422. https://doi.org/10.1175/1520-0469(1989)046<0410:tspwsa>2.0.co;2

Jacobi, C. (2014). Long-term trends and decadal variability of upper mesosphere/lower thermosphere gravity waves at midlatitudes. *Journal of Atmospheric and Solar-Terrestrial Physics*, *118*, 90–95. https://doi.org/10.1016/j.jastp.2013.05.009

Kawahara, T. D., Gardner, C. S., & Nomura, A. (2004). Observed temperature structure of the atmosphere above Syowa Station, Antarctica (69oS, 39oE). *Journal of Geophysical Research*, *109*, D12103. https://doi.org/10.1029/2003JD003918

Krueger, D. A., She, C.-Y., & Yuan, T. (2015). Retrieving mesopause temperature and line-of-sight wind from full-diurnal-cycle Na lidar observations. *Applied Optics*, *54*(32), 9469–9489. https://doi.org/10.1364/AO.54.009469

Lautenbach, J., & Höffner, J. (2004). Scanning iron temperature lidar for mesopause temperature observations. *Applied Optics*, *43*, 4559–4563. https://doi.org/10.1364/AO.43.004559

Li, T., Leblanc, T., McDermid, I. S., Wu, D. L., Dou, X., & Wang, S. (2010). Seasonal and interannual variability of gravity wave activity revealed by long-term lidar observations over Mauna Loa Observatory, Hawaii. *Journal of Geophysical Research*, *115*, D13103. https://doi.org/10.1029/2009JD013586

Lindzen, R. S. (1981). Turbulence and stress owing to gravity wave and tidal breakdown. *Journal of Geophysical Research*, *86*, 9707–9714. https://doi.org/10.1029/jc086ic10p09707

Liu, X., Yue, J., Xu, J., Garcia, R. R., Russell, J. M., III, Mlynczak, M., et al. (2017). Variations of global gravity waves derived from 14 years of SABER temperature observations. *Journal of Geophysical Research: Atmospheres*, *122*, 6231–6249. https://doi.org/10.1002/2017JD026604

Lübken, F.-J., & von Zahn, U. (1991). Thermal structure of the mesopause in summer region at polar latitudes. *Journal of Geophysical Research*, *96*, 20841–20857.

Mzé, N., Hauchecorne, A., Keckhut, P., & Thétis, M. (2014). Vertical distribution of gravity wave potential energy from long-term Rayleigh lidar data at a northern middle-latitude site. *Journal of Geophysical Research: Atmospheres*, *119*, 12069–12083. https://doi.org/10.1002/2014JD022035

Nakamura, T., Tsuda, T., Fukao, S., Vincent, A. H., Meek, C. E., Vincent, R. A., et al. (1996). Mesospheric gravity waves at Saskatoo (52N0, Kyoto (35N) and Adelaide (35S). *Journal of Geophysical Review.*, *101*, 7005–7012. https://doi.org/10.1029/95jd03826

Pan, W., & Gardner, C. S. (2003). Seasonal variations of the atmospheric temperature structure at South Pole. *Journal of Geophysical Research*, *108*(D18), 4564. https://doi.org/10.1029/2002JD003217

Rauthe, M., Gerding, M., & Lubken, F. J. (2008). Seasonal changes in gravity wave activity measured by lidars at mid-latitudes. *Atmospheric Chemistry and Physics*, *8*, 6775–6787. www.atmos-chem-phys.net/8/6775/2008/

She, C. Y., Berger, U., Yan, Z.-A., Yuan, T., Lübken-J, F., Krueger, D. A., et al. (2019). Solar response and long-term trend of midlatitude mesopause region temperature based on 28 Years (1990–2017) of Na lidar observations. *Journal of Geophysical Research: Space Physics*, *124*, 7140–7156. https://doi.org/10.1029/2019JA026759

She, C. Y., Chen, S.-S., Hu, Z.-L., Sherman, J., Vance, J. D., Vasoli, V., et al. (2000). Eight-year climatology of nocturnal temperature and sodium density in the mesopause region (80 to 105 km) over Fort Collins, CO (41oN, 105oW). *Geophysical Research Letters*, *27*, 3289–3292. https://doi.org/10.1029/2000gl003825

She, C. Y., & Krueger, D. A. (2007). Laser-induced fluorescence: Spectroscopy in the sky. *Optics & Photonic News*, *18*(9), 35–41. https://doi.org/10.1364/opn.18.9.000035

She, C.-Y., Krueger, D. A., & Yuan, T. (2015). Long-term midlatitude mesopause region temperature trend deduced from quarter century (1990–2014) Na lidar observations. *Annals of Geophysics*, *33*, 363–369. https://doi.org/10.5194/angeo-33-363-2015

She, C. Y., Latifi, H., Yu, J. R., Alvarez, R. J., II, Bills, R. E., & Gardner, C. S. (1990). Two-frequency lidar technique for mesospheric Na temperature measurements. *Geophysical Research Letters*, *17*, 929–932. https://doi.org/10.1029/gl017i007p00929

She, C. Y., Liu, A. Z., Yuan, T., Yue, J., Li, T., Ban, C., & Friedman, J. S. (2021). MLT science enabled by atmospheric lidars. In W. Wang, Y. Zhang, & L. J. Paxton (Eds.), *Upper atmospheric dynamics and energetics, space physics and aeronomy collection*, (Vol. 4). John Wiley and Sons, https://doi.org/10.1002/9781119815631.ch20

She, C. Y., Thiel, S. W., & Krueger, D. A. (1998). Observed episodic warming at 86 and 100 km between 1990 and 1997: Effects of Mount Pinatubo eruption. *Geophysical Research Letters*, *25*(4), 497–500. https://doi.org/10.1029/98GL00178

She, C. Y., & von Zahn, U. (1998). The concept of two-level mesopause: Support through new lidar observation. *Journal of Geophysical Research*, *103*, 5855–5863. https://doi.org/10.1029/97jd03450

She, C.-Y., & Yu, J. R. (1994). Simultaneous three-frequency Na lidar measurements of radial wind and temperature in the mesopause region. *Geophysical Research Letters*, *21*, 1771–1774. https://doi.org/10.1029/94gl01417

She, C. Y., Yu, J. R., & Chen, H. (1993). Observed thermal structure of a midlatitude mesopause. *Geophysical Research Letters*, *20*, 567–570. https://doi.org/10.1029/93gl00808

She, C. Y., Yu, J. R., Krueger, D. A., Roble, R., Keckhut, P., Hauchecome, A., et al. (1995). Vertical structure of the midlatitude temperature from stratosphere to mesosphere (30-105 km). *Geophysical Research Letters*, *22*, 377–380. https://doi.org/10.1029/95gl00010

States, R. J., & Gardner, C. S. (2000). Thermal structure of the mesopause region (80–105 km) at 40oN latitude. Part I: Seasonal Variations. *Journal of the Atmospheric Sciences*, *57*, 66–77.

Strelnikova, I., Almowafy, M., Baumgarten, G., Baumgarten, K., Ern, M., Gerding, M., & Lübken, F.-J. (2021). Seasonal cycle of gravity wave potential energy densities from Lidar and satellite observations at 54° and 69°N. *Journal of the Atmospheric Sciences*, *78*, 1359–1386. https://doi.org/10.1175/JAS-D-20-0247.1

Vadas, S. L., & Becker, E. (2019). Numerical modeling of the generation of tertiary gravity waves in the mesosphere and thermosphere during strong mountain wave events over the Southern Andes. *Journal of Geophysical Research: Space Physics*, *124*, 7687–7718. https://doi.org/10.1029/2019JA026694

Van Zandt, T. E., & Fritts, D. C. (1989). A theory of enhanced saturation of the gravity wave spectrum due to increases in atmospheric stability. *Pure and Applied Geophysics*, *130*, 399–420. https://doi.org/10.1007/BF00874466

von Zahn, U., & Höffner, J. (1996). Mesopause temperature profiling by potassium lidar. *Geophysical Research Letters*, *23*, 141–144. https://doi.org/10.1029/95gl03688

Whiteway, J. A., & Carswell, A. I. (1995). Lidar observations of gravity wave activity in the upper stratosphere over Toronto. *Journal of Geophysical Research*, *100*(D7), 14113–14124. https://doi.org/10.1029/95JD00511

Williams, A. P., Cook, B. I., & Smerdon, J. E. (2022). Rapid intensification of the emerging southwestern North American megadrought in 2020–2021. *Nature Climate Change*. https://doi.org/10.1038/s41558-022-01290-z

Wilson, R., Chanin, M. L., & Hauchecorne, A. (1991). Gravity waves in the middle atmosphere observed by Rayleigh lidar: 1. Case studies. *Journal of Geophysical Research: Atmospheres*, *96*, 5153–5167. https://doi.org/10.1029/90JD02231

Yu, J.-R., & She, C.-Y. (1995). Climatology of a midlatitude mesopause region observed by a lidar at Fort Collins, Colorado (40.6oN, 105oW). *Journal of Geophysical Research*, *100*, 7441–7452. https://doi.org/10.1029/94jd03109

Yuan, T., She, C.-Y., Krueger, D. A., Sassi, F., Garcia, R., Roble, R., et al. (2008). Climatology of mesopause region temperature, zonal wind and meridional wind over Fort Collins, CO (41ºN, 105ºW) and comparison with model simulations. *Journal of Geophysical Research*, *113*, D03105. https://doi.org/10.1029/2007JD008697

Yue, X., Friedman, J. S., Zhou, Q.-H., Wu, X.-B., & Lautenbach, J. (2018). Long-term lidar observations of the gravity wave activity near the mesopause at Arecibo. *Atmospheric Chemistry and Physics Discussions*. https://doi.org/10.5194/acp-2018-731